

Syddansk Universitet

Direct Characterization of Plasmonic Slot Waveguides and Nanocouplers

Andryieuski, Andrei; Zenin, Volodymyr; Malureanu, Radu; Volkov, Valentyn S.; Bozhevolnyi, Sergey I.; Lavrinenko, Andrei V.

Published in:
Nano Letters

DOI:
[10.1021/nl501207u](https://doi.org/10.1021/nl501207u)

Publication date:
2014

Document Version
Publisher's PDF, also known as Version of record

[Link to publication](#)

Citation for pulished version (APA):

Andryieuski, A., Zenin, V., Malureanu, R., Volkov, V. S., Bozhevolnyi, S. I., & Lavrinenko, A. V. (2014). Direct Characterization of Plasmonic Slot Waveguides and Nanocouplers. *Nano Letters*, 14(7), 3925-3929. DOI: 10.1021/nl501207u

General rights

Copyright and moral rights for the publications made accessible in the public portal are retained by the authors and/or other copyright owners and it is a condition of accessing publications that users recognise and abide by the legal requirements associated with these rights.

- Users may download and print one copy of any publication from the public portal for the purpose of private study or research.
- You may not further distribute the material or use it for any profit-making activity or commercial gain
- You may freely distribute the URL identifying the publication in the public portal ?

Take down policy

If you believe that this document breaches copyright please contact us providing details, and we will remove access to the work immediately and investigate your claim.

Direct Characterization of Plasmonic Slot Waveguides and Nanocouplers

Andrei Andryieuski,^{*,†} Vladimir A. Zenin,^{*,‡} Radu Malureanu,[†] Valentyn S. Volkov,[‡] Sergey I. Bozhevolnyi,[‡] and Andrei V. Lavrinenko[†]

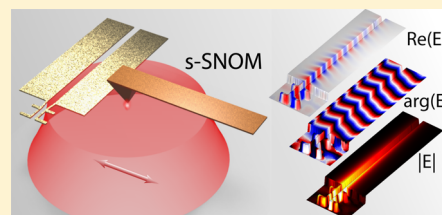
[†]DTU Fotonik, Technical University of Denmark, Ørstedss pl. 343, Kongens Lyngby DK-2800, Denmark

[‡]Department of Technology and Innovation, University of Southern Denmark, Niels Bohrs Allé 1, Odense M DK-5230, Denmark

S Supporting Information

ABSTRACT: We demonstrate the use of amplitude- and phase-resolved near-field mapping for direct characterization of plasmonic slot waveguide mode propagation and excitation with nanocouplers in the telecom wavelength range. We measure mode's propagation length, effective index and field distribution and directly evaluate the relative coupling efficiencies for various couplers configurations. We report 26- and 15-fold improvements in the coupling efficiency with two serially connected dipole and modified bow-tie antennas, respectively, as compared to that of the short-circuited waveguide termination.

KEYWORDS: Nanocoupler, surface plasmon, slot waveguide, nanoantenna, s-SNOM, near-field microscopy



Great advantages offered by plasmonics to optical waveguiding are extreme subwavelength localization of guided modes close to the metal interface¹ together with electrical tunability of electromagnetic waves via intrinsic metallic contacts.² Plasmonic waveguides are therefore considered as a future generation of optical interconnects in integrated circuits for datacom technologies.³ Inevitably, with the appearance of nanoscale waveguides a new challenge has emerged: how to effectively couple the diffraction-limited optical waves into deep-subwavelength plasmonic waveguides. Various approaches have been utilized ranging from lenses to grating couplers.⁴ However, the most compact solution is an antenna-based nanocoupler.

Antenna is a common tool to capture free-space propagating radio-waves with more than a century-long history.⁵ Employment of metal-based antennas in photonics started only in the last two decades owing to the progress in high-resolution nanofabrication techniques.^{6,7} Usage of plasmonic antennas⁸ to couple light to plasmonic waveguides has been suggested theoretically^{9–15} and then confirmed experimentally with cross-polarization microscopy measurements in the near-infrared¹⁶ and with near-field microscopy in optical,¹⁷ telecom,¹⁸ and mid-infrared¹⁹ ranges. Nevertheless, the amplitude- and phase-resolved measurements of the antenna-excited slot plasmons in the telecom range (with the free-space wavelength around 1.55 μm) have not been reported so far. It should be emphasized that the usage of phase-resolved near-field mapping is indispensable for direct characterization of the mode effective index as well as for revealing the symmetry of excited plasmonic modes.¹⁹

In this Letter, we report for the first time to our knowledge the amplitude- and phase-resolved near-field characterization of plasmonic slot waveguides and antenna-based nanocouplers in the telecom wavelength range. Illumination with a wide laser

beam excites both slot plasmons confined within a dielectric gap in a metal film and surface plasmon polaritons (SPP) propagating along the metal film interface perpendicular to the slot, and the resulting near-field interference pattern is mapped with a scattering-type scanning near-field optical microscope (s-SNOM). The observed interference pattern undergoes then the special filtration procedure in order to extract individual characteristics of the slot mode, including the effective index and propagation length, and its relative excitation efficiency, which is determined as a ratio between the slot mode intensity at the waveguide input and the average SPP intensity. Experimental characterization of two serial dipole and modified bow-tie antennas as well as the short-circuited waveguide termination in the absence of any coupling device is related to modeling of these configurations, including calculations of propagating mode fields and effective areas.

We use a plasmonic slot waveguide²⁰ (also known as a gap or channel waveguide), representing a rectangular slot of width $W_{\text{WG}} = 300$ nm carved in a gold film of thickness $H = 50$ nm. Such a waveguide features both reasonably good mode confinement and propagation length. In a symmetric dielectric environment, the propagation length can reach few tens of micrometers at telecom wavelengths. We, however, select an asymmetric configuration (Figure 1a, inset) that allows one to directly map plasmonic mode-field distributions with a sharp probe tip of the s-SNOM. The drawback of such a configuration is the energy leakage from the slot mode to the slow SPPs on the silica–gold interface (the effective index of the latter is larger than that of the former). The leakage losses

Received: April 1, 2014

Revised: May 28, 2014

Published: June 2, 2014

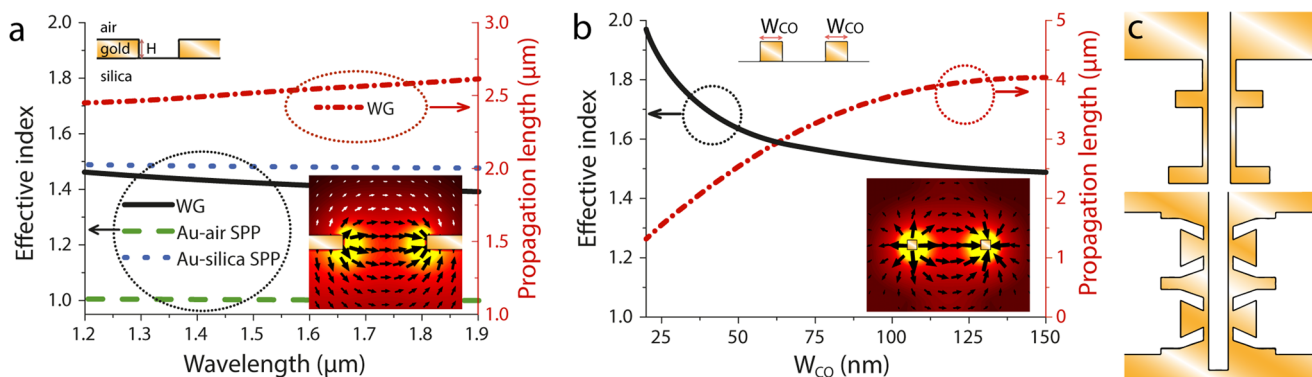


Figure 1. (a) Effective indices of the slot waveguide mode (black solid line), gold–air (green dashed) and gold–silica (blue dotted) SPPs together with the propagation length of the slot mode (red dashed-dotted). (b) Effective index (black) and propagation length (red dashed-dotted) of the transmission line waveguide mode depending on the wire width W_{CO} . Two serially connected (c) dipole and (d) modified bow-tie antennas. Insets in (a) and (b) show cross sections of the correspondent waveguides geometry and total electric field magnitude distributions of the plasmonic modes.

add up to the ohmic losses in the plasmonic waveguide, resulting in the propagation length of $\sim 2.5 \mu\text{m}$ (Figure 1a). However, simulations indicate that it is sufficient to fill the slot space and add an additional 50 nm thick layer of silica on top in order to eliminate the leakage losses and increase the propagation length up to $\sim 7 \mu\text{m}$. For comparison, the propagation lengths of the air–gold and silica–gold SPPs are 230 and $63 \mu\text{m}$, respectively, at the wavelength $1.55 \mu\text{m}$.

In our previous work,⁹ we showed that the serial connection of the antennas provides no benefits for the slot excitation with the tightly focused Gaussian beam, whereas it is an opposite case for the incident plane wave or wide Gaussian beam used in our experimental setup. It is, therefore, important to ensure the optimal connection between the nanoantennas to deliver maximum of the incident energy to the waveguide. The effective index and propagation length of the double-wire transmission line depends on the wire width W_{CO} (Figure 1b). Smaller losses correspond to wider wires, but wide wires connected to the antenna would prohibit efficient plasmons excitation. It is therefore better to increase the width of the connecting wires in the regions between the antennas, while keeping them narrow otherwise. In order to check the advantage of wider wires we compare thin-wire-connected dipole antennas (Figure 1c) with modified bow-tie antennas that feature widened wire sections between them (Figure 1d). To prevent the wide regions from out-of-phase plasmons excitation, we tune the length of the wide sections out of the resonance.

Numerical simulation and optimization of the nanocouplers for operation at the wavelength of $1.55 \mu\text{m}$ (see Supporting Information for details) was carried out in CST Microwave Studio.²¹ For the plane wave excitation (normal to the substrate in our case), the figure-of-merit of the antenna, which characterizes its coupling efficiency and which is used as an objective function during optimization, is its effective area defined as the ratio of the power delivered to a waveguide mode to the incident power flux $A_{\text{eff}} = P_{\text{WG}}/S_{\text{inc}}$. The effective area of one (1DA), two (2DA), and three (3DA) dipole antenna couplers was calculated and found being considerably and progressively larger than that of the open circuit waveguide termination (0DA) (Figure 2, Table 1). At the same time, the operation full width at half-maximum (fwhm) bandwidth of the 3DA coupler is smaller than that of the 2DA one. This fact agrees with the usual trade-off between antenna efficiency and bandwidth. The advantage of larger plasmon propagation

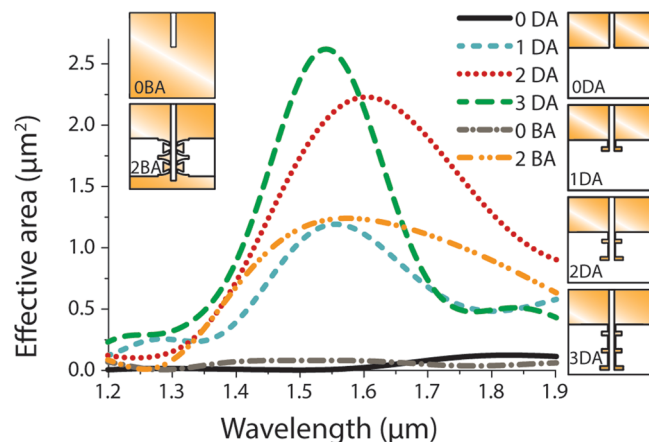


Figure 2. Effective area of open circuit waveguide (0DA, black solid), one (1DA, cyan short-dashed), two (2DA, red dotted), and three (3DA, green long-dashed) serial dipoles, short-circuited waveguide (0BA, gray dashed-dotted) and two serial modified bow-tie (2BA, orange dashed-double-dotted) antennas. It is seen that the effective area A_{eff} increases with the number of antennas. The values A_{eff} at the wavelength of $1.55 \mu\text{m}$ are collected in Table 1.

Table 1. Bandwidth of the Nanocouplers and Their Effective Area at the Optimization Wavelength $1.55 \mu\text{m}$

design	$A_{\text{eff}} (\mu\text{m}^2)$	bandwidth (μm)
0 DA	0.0070	
1 DA	1.19	0.30
2 DA	2.09	0.39
3 DA	2.61	0.22
0 BA	0.081	0.38
2 BA	1.23	0.62

length in wider connecting wires does not compensate for worse plasmon excitation due to interaction of metallic bars with the antenna elements and their detuning as well as counter-phase slot plasmons excitation in the modified bow-tie (2BA) antennas, resulting in ~ 1.7 times smaller effective area, but ~ 1.5 times larger bandwidth with respect to that of 2DA. The short-circuited waveguide termination (0BA) was found to be significantly more (by 1 order of magnitude) efficient for slot plasmon excitation than the 0DA configuration. Such a large difference in the coupling efficiencies can be explained by the difference in the corresponding excitation channels; in the 0BA

case, the waveguide mode is excited by directional light scattering from a metallic edge extending over the whole waveguide width, whereas in the ODA case it is only excited by scattering off metallic corners with most of scattered light propagating away from the waveguide entrance. Bearing this in mind, we selected the OBA configuration for the experimental fabrication and characterization together with the 2BA and 2DA cases that promise, respectively, 15- and 26-fold improvements in the effective area A_{eff} at the wavelength 1.55 μm (Table 1).

The nanocouplers were fabricated using standard electron-beam (e-beam) lithography followed by metal e-beam evaporation and lift-off in acetone (see Supporting Information for details).

Phase- and amplitude-resolved near-field characterization of the plasmonic antenna nanocouplers was carried out using the s-SNOM configuration, based on an atomic force microscope (AFM) with cantilevered tips being employed as near-field probes (NeasNOM from Neaspec GmbH) (Figure 3). In our

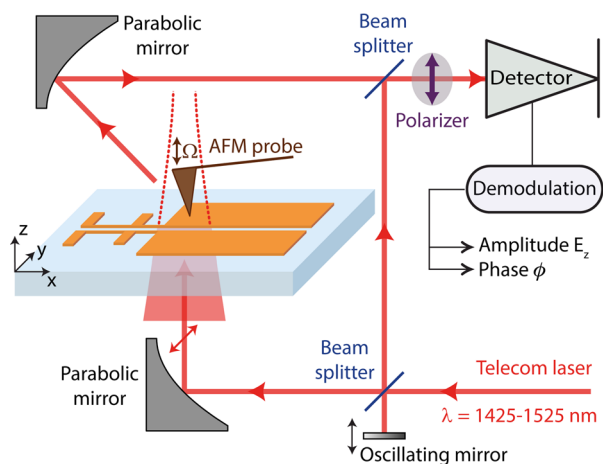


Figure 3. Schematic of amplitude and phase near-field mapping with the transmission s-SNOM setup. The sample is illuminated from below with a defocused laser beam (fwhm $\sim 12 \mu\text{m}$) polarized parallel to the dipole antenna. The AFM metal-covered silicon tip scatters the near field (predominantly its vertical component), and the scattered radiation (being collected by the top parabolic mirror) is then mixed with the reference beam and interferometrically detected, yielding amplitude and phase near-field distributions by scanning the sample.

experiments, we used standard commercial Si tips covered with platinum (Arrow NCPT, NanoWorld). The AFM was operated in the tapping mode with the tip oscillating at the mechanical

resonance frequency $\Omega \approx 250 \text{ kHz}$ with the amplitude of $\sim 50 \text{ nm}$. Near-field and topography mapping was performed by moving the sample across the aligned configuration of the oscillating tip and the illumination system. Therefore, in order to continuously excite the antenna we illuminated the structures from below (transmission-mode s-SNOM²²) with a defocused polarized laser beam (the estimated fwhm illumination spot was $\sim 12 \mu\text{m}$). The light, scattered by the tip, was collected by a top parabolic mirror and directed toward a detector, where it was spatially overlapped with an interfering reference beam, yielding both the amplitude and phase of the scattered light via pseudoheterodyne detection.²³ Background contributions were suppressed by demodulating the detector signal at a high-order harmonic frequency $n\Omega$ (in our case $n = 2$), providing background-free near-field amplitude and phase images. It should be pointed out that in most s-SNOM experiments the illumination is done in the reflection mode (side-illumination scheme), where the incident light is focused on the tip with the same parabolic mirror that collects scattered light, a configuration that creates many problems for obtaining clear near-field images due to strong tip-sample coupling²⁴ and phase-retardation effects.²⁵ However, in our transmission-mode configuration the sample was illuminated from below with an in-plane direction of polarization, allowing us to achieve uniform illumination and efficient excitation of the plasmonic antenna while avoiding the direct tip excitation.^{22,25,26} Because of a dominating dipole moment of the tip along its axis (i.e., along the z -axis), the recorded s-SNOM images represent mostly a distribution of the amplitude and phase of the z -component of the electric field, E_z .²⁵ In order to enhance this selectivity, a polarizer in front of the detector was set to select the out-of-plane z -polarization of light scattered by the tip. Finally, the recorded data were treated with free (scanning probe microscopy) software Gwyddion.²⁷

The recorded optical amplitude and phase images (Figure 4b,c) exhibit a complex interference pattern, produced mainly by the slot waveguide mode and SPPs. The latter are excited with the incident wave being diffracted on the slot, and propagate away from and perpendicular to the slot waveguide. Because of the large (defocused) excitation laser spot, adjusted with the AFM tip during the scan, the SPP amplitude and phase do not significantly change along the waveguide, as opposed to those of the slot mode. One can therefore decompose the recorded raw near-field data (Figure 4b–d) in the half-space containing the waveguide into the SPP background (Figure 4e–g) and slot mode (Figure 4h–j) fields by fitting the data along the waveguide as a sum of propagating mode and a constant background (see Supporting Information for details).

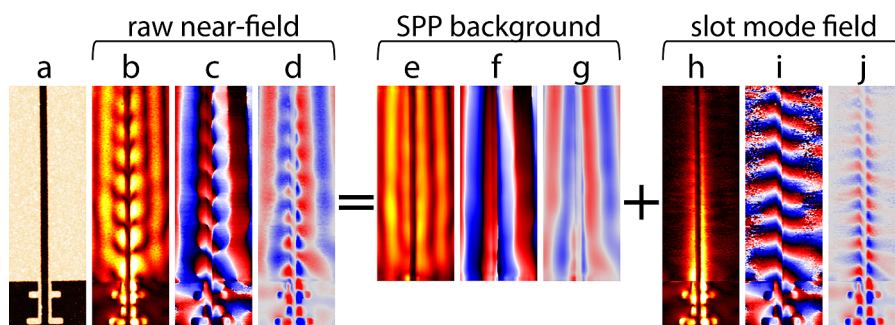


Figure 4. Pseudocolor s-SNOM images, representing (a) topography, (b) amplitude, (c) phase, and (d) real part of the raw optical near-field distribution. Amplitude, phase, and real part of the decomposed contributions of (e–g) SPP background and (h–j) slot mode fields.

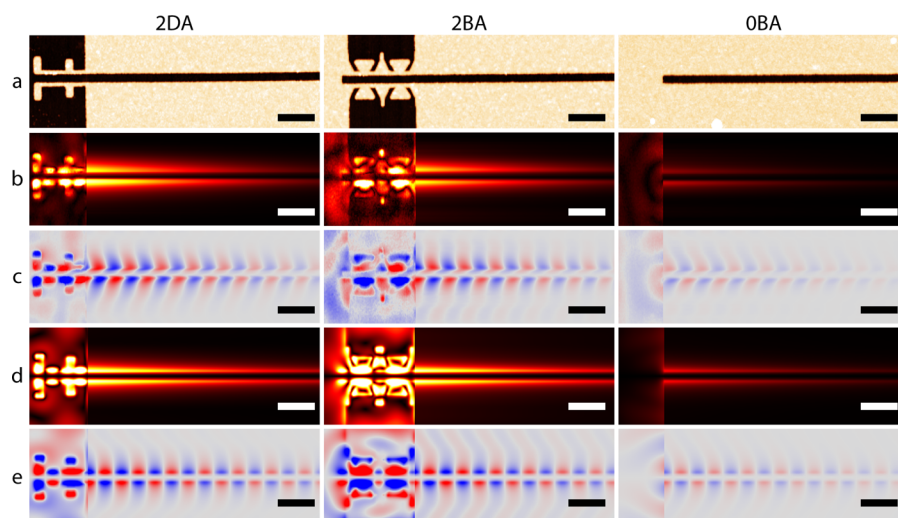


Figure 5. Pseudocolor s-SNOM images, representing (a) topography, filtered (b) amplitude, and (c) real part of measured near-field data, and filtered (d) amplitude and (e) real part of simulated field for all three types of nanocouplers: 2DA (left), 2BA (middle), and OBA (right). Electric field of the slot mode is normalized to the average amplitude of the background SPP. The scale bar is equal to 1 μm .

Thus, filtered images reveal the propagating slot mode with the decreasing amplitude (Figure 4h) and linearly advancing phase (Figure 4i) of E_z field. As expected from the mode-field distribution (Figure 1a, inset), E_z field magnitude is zero in the middle and opposite in sign on both sides of the waveguide (Figure 4j).

The filtering procedure was applied to all measurements (see Supporting Information for more details) made in the telecom range (1425–1525 nm) and to all three types of antenna nanocouplers: 2DA, 2BA, and OBA (Figure 5b,c). Numerically simulated E_z field distribution at the height of 50 nm above the structure (the average position of the s-SNOM tip) was filtered with the same procedure (Figure 5d,e), signifying very reasonable agreement with the experimental results. We should mention that phase images not only allow observing slot plasmon phase evolution but also reveal information on the impedance matching of the antennas to the waveguide.

The filtered images of the slot mode allowed us to estimate the effective mode index, propagation length and intensity of the slot mode at the waveguide entrance (Figure 6) normalized to the average intensity of the SPP background, which does not significantly depend on the wavelength in the range of 1.425–1.525 μm . Thus, normalized slot mode intensity is expected to be proportional to the nanocoupler effective area $I_{\text{slot at } x=0} \sim P_{\text{WG}} \sim A_{\text{eff}}$. The validation of such approach is supported by the comparison of simulation results (lines) with experimental results (points), shown in Figure 6a. The effective indices determined from the experimental (filtered) phase images (Figure 5c) were found in good correspondence with the calculated ones (Figure 6b), while the experimentally obtained propagation lengths turned out being slightly smaller than the calculated ones (Figure 6b), most probably due to the fabrication imperfections. One may notice small oscillations in the experimentally measured values, which, we believe represent a systematic error due to degradation or a drift in our setup, because a sequence of measurements for each antenna was 1475–1425–1525–1500–1450 nm, which correlates well with the error in propagation length and effective index (Figure 6b).

In conclusion, we have demonstrated the use of amplitude- and phase-resolved near-field mapping for complete character-

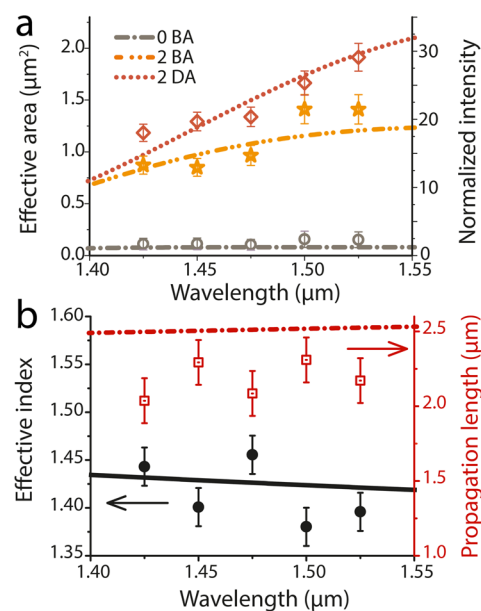


Figure 6. (a) Wavelength dependence of the coupling efficiency of different type of antennas: OBA (gray, circles), 2BA (orange, stars), and 2DA (red, rhombs), represented as effective area for numerical calculations (lines) and as normalized intensity for experimental results (points). (b) Wavelength dependence of the experimentally measured effective mode index (black circles) and propagation length (red squares), compared with numerical simulations (lines).

ization of the complex plasmonic waveguide configuration including antenna-based nanocouplers and slot waveguides. The s-SNOM characterization allowed us not only to make relative comparison of the efficiencies (in terms of the effective area) of different couplers but also to measure the effective index and propagation length of the slot waveguide mode. All experimental data were found to be in a very good correspondence with the numerical simulations. We have also confirmed that the serially connected dipole antennas represent the most efficient (for the excitation with a wide light beam) and simple design of nanocouplers. We would therefore anticipate that the serial antennas nanocouplers will become

efficient optical interfaces between macroscopic light sources and nanoscale waveguides. We also believe that the s-SNOM-based characterization procedure described here will become a standard robust technique for the plasmonic waveguide characterization due to its high resolution, reliable measurements, and efficient data filtration procedure.

■ ASSOCIATED CONTENT

■ Supporting Information

Details on numerical simulation and optimization, and the fabrication procedure and the filtration procedure for experimental and simulated field distributions. This material is available free of charge via the Internet at <http://pubs.acs.org>.

■ AUTHOR INFORMATION

Corresponding Authors

*E-mail: andra@fotonik.dtu.dk.

*E-mail: zenin@iti.sdu.dk.

Author Contributions

A. A. and V. Z. contributed equally.

Notes

The authors declare no competing financial interest.

■ ACKNOWLEDGMENTS

A.A. acknowledges financial support from the Danish Council for Technical and Production Sciences through the GraTer project (Contract No. 0602-02135B). V.A.Z., V.S.V., and S.I.B. acknowledge financial support from the Danish Council for Independent Research (the FTP project ANAP, Contract No. 0602-01507B) and from the European Research Council, Grant 341054 (PLAQNAP). The authors also acknowledge J. Rosenkrantz de Lasson for a useful discussion on numerical simulations, G. Biagi, T. Holmgaard, J.-S. Bouillard, and A. V. Zayats for discussions on near-field characterization, and an anonymous reviewer for useful comments.

■ REFERENCES

- (1) Gramotnev, D. K.; Bozhevolnyi, S. I. *Nat. Photonics* **2010**, *4*, 83–91.
- (2) MacDonald, K. F.; Zheludev, N. I. *Laser Photonics Rev.* **2009**, *4*, 562–567.
- (3) Ozbay, E. *Science* **2006**, *311*, 189–193.
- (4) Andryieuski, A.; Lavrinenko, A. V. *Adv. OptoElectron.* **2012**, *2012*, 1–17.
- (5) Bharadwaj, P.; Deutsch, B.; Novotny, L. *Adv. Opt. Photonics* **2009**, *438*–483.
- (6) Henzie, J.; Lee, J.; Lee, M. H.; Hasan, W.; Odom, T. W. *Annu. Rev. Phys. Chem.* **2009**, *60*, 147–165.
- (7) Boltasseva, A.; Shalae, V. *Metamaterials* **2008**, *2*, 1–17.
- (8) Krasnok, A. E.; Maksymov, I. S.; Denisyuk, A. I.; Belov, P. A.; Miroshnichenko, A. E.; Simovski, C. R.; Kivshar, Y. S. *Phys.-Usp.* **2013**, *56*, 539–564.
- (9) Andryieuski, A.; Malureanu, R.; Biagi, G.; Holmgaard, T.; Lavrinenko, A. *Opt. Lett.* **2012**, *37*, 1124–1126.
- (10) Wen, J.; Romanov, S.; Peschel, U. *Opt. Express* **2009**, *17*, 5925–5932.
- (11) Huang, J.; Feichtner, T.; Biagioni, P.; Hecht, B. *Nano Lett.* **2009**, *9*, 1897–1902.
- (12) Fang, Z.; Lu, Y.; Fan, L.; Lin, C. *Plasmonics* **2010**, *5*, 57–62.
- (13) Klemm, M. *Int. J. Opt.* **2012**, *2012*, 1–7.
- (14) Obelleiro, F.; Taboada, J. M.; Solís, D. M.; Bote, L. *Opt. Lett.* **2013**, *38*, 1630–1632.
- (15) Alu, A.; Engheta, N. *Phys. Rev. Lett.* **2010**, *104*, 213902.
- (16) Wen, J.; Banzer, P.; Kriesch, A.; Ploss, D.; Schmauss, B.; Peschel, U. *Appl. Phys. Lett.* **2011**, *98*, 101109.
- (17) Fang, Z.; Fan, L.; Lin, C.; Zhang, D.; Meixner, A. J. A. J.; Zhu, X. *Nano Lett.* **2011**, *11*, 1676–1680.
- (18) Kriesch, A.; Burgos, S. P.; Ploss, D.; Pfeifer, H.; Atwater, H. A.; Peschel, U. *Nano Lett.* **2013**, *13*, 4539–4545.
- (19) Schnell, M.; Alonso-Gonzalez, P.; Arzubaga, L.; Casanova, F.; Hueso, L. E.; Chuvilin, A.; Hillenbrand, R. *Nat. Photonics* **2011**, *5*, 283–287.
- (20) Veronis, G.; Fan, S. J. *Light. Technol.* **2007**, *25*, 2511–2521.
- (21) CST. Computer Simulation Technology, AS <http://cst.com> (accessed June 3, 2014).
- (22) Schnell, M.; Garcia-Etxarri, A.; Huber, A. J.; Crozier, K. B.; Borisov, A.; Aizpurua, J.; Hillenbrand, R. J. *Phys. Chem. C* **2010**, *114*, 7341–7345.
- (23) Ocelic, N.; Huber, A.; Hillenbrand, R. *Appl. Phys. Lett.* **2006**, *89*, 101124.
- (24) García-Etxarri, A.; Romero, I.; García de Abajo, F.; Hillenbrand, R.; Aizpurua, J. *Phys. Rev. B* **2009**, *79*, 125439.
- (25) Esteban, R.; Vogelgesang, R.; Dorfmueller, J.; Dmitriev, A.; Rockstuhl, C.; Etrich, C.; Kern, K. *Nano Lett.* **2008**, *8*, 3155–3159.
- (26) Schnell, M.; Garcia-Etxarri, A.; Huber, A.; Crozier, K. B.; Aizpurua, J.; Hillenbrand, R. *Nat. Photonics* **2009**, *3*, 287–291.
- (27) Gwyddion, <http://gwyddion.net/> (accessed June 3, 2014).

Direct Characterization of Plasmonic Slot Waveguides and Nanocouplers

Andrei Andryieuski^{†}, Vladimir A. Zenin^{‡*}, Radu Malureanu[†], Valentyn S. Volkov[‡], Sergey I. Bozhevolnyi[‡], and Andrei V. Lavrinenko[†]*

[†]DTU Fotonik, Technical University of Denmark, Ørstedssø pl. 343, Kongens Lyngby DK-2800, Denmark

[‡]Department of Technology and Innovation, University of Southern Denmark, Niels Bohrs Alle 1, Odense M DK-5230, Denmark

* E-mail: andra@fotonik.dtu.dk

* E-mail: zenin@iti.sdu.dk

Supporting information

Numerical simulation and optimization. Simulations are done in CST Microwave Studio¹ with the time-domain finite-integrals method. A hexahedral mesh with the mesh refinement around the slot waveguide is used. The simulation domain consists of a thick silica substrate (3 μm), waveguide, antenna and thick air superstrate (4 μm) (Figure S1a). Gold is described with the Drude formula² with plasma frequency $1.36 \times 10^{16} \text{ s}^{-1}$ and collision frequency $1.57 \times 10^{14} \text{ s}^{-1}$. The dielectric substrate has a refractive index $n = 1.47$. A plane wave is used for the excitation

of the structure. The boundary conditions are perfect electric conductor (PEC) in the x-, and open (perfectly matched layers) in y- and z-directions. To ensure the absence of coupling to the mirror images of antennas at the PEC x- boundaries, the lateral size of the simulation domain is $11\ \mu\text{m}$, the longitudinal size is $9\ \mu\text{m}$ (for calculations of the effective area and optimization) or $19\ \mu\text{m}$ (for calculations of the electromagnetic fields). Typical simulation with a 12 CPUs (3.5 GHz), 48 GB RAM personal computer takes 1 hour. Numerical optimization with maximization of the effective area as a goal was done with the Nelder-Mead simplex algorithm with the parameters variation range $\pm 25\%$ from the initial values. The initial values were selected through maximization of the effective area for all parameters one-by-one variation. The optimal parameters are shown in Table S1 with the geometrical parameters marked in Figure S1b,c.

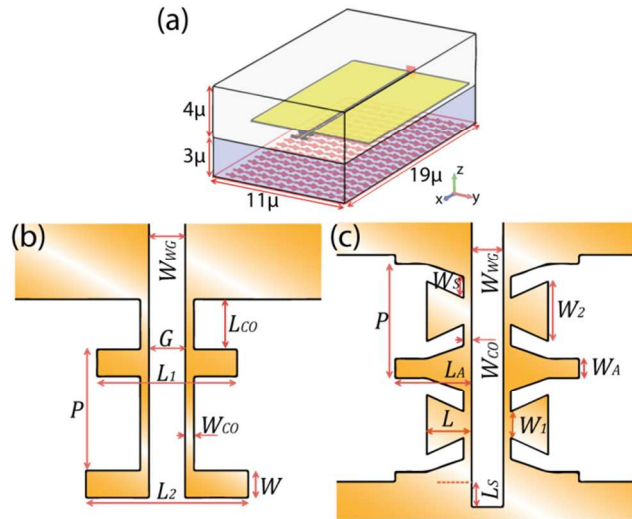


Figure S1. (a) Simulation domain used for the fields calculation in CST Microwave Studio. In case of effective area calculation the longitudinal size of the domain was $9\ \mu\text{m}$ instead of $19\ \mu\text{m}$. Optimized serially connected (b) dipole and (c) modified bow-tie antennas. The values of optimal geometrical parameters are presented in the Table S1.

Initially we observed spurious Fabry-Perot resonances in the effective area spectra due to poorly absorbed scattered field by a single-mode plane wave port in CST (the excitation plane wave is shown with arrows in Figure S1a). This issue has been resolved by increasing the number of the port modes to 20 and proper time windowing of the received signal. The electric field recorded with a frequency 3D monitor was collected 50 nm above the top waveguide surface, corresponding to the average position of the s-SNOM tip in experiments. In order to reduce the influence of the fake Fabry-Perot resonances on the simulated electric field, the width of the excitation port was decreased to 4 μm .

Table S1. Waveguide and nanocouplers geometrical parameters, designed and fabricated.

Parameter	Designed	Fabricated	St. deviation
All structures			
H (nm)	50	50	1
Waveguide			
W_{WG} (nm)	300	287	7
Dipole antennas coupler (2DA)			
L_1 (nm)	1144	1117	8
L_2 (nm)	1290	1293	10
G (nm)	290	288	5
W (nm)	210	213	6
L_{CO} (nm)	443	396	10
W_{CO} (nm)	80	82	8
P (nm)	969	969	8
Bow-tie antenna coupler (2BA)			
L (nm)	437	425	10
W_1 (nm)	233	246	12
W_2 (nm)	560	562	13
L_A (nm)	683	647	7

W_A (nm)	70	74	11
W_{CO} (nm)	76	74	8
W_S (nm)	230	200	17
L_S (nm)	230	234	4
P (nm)	1069	1071	20

Upon the incident wave's diffraction through the slot the surface plasmon polaritons (SPPs) are excited on the metal-dielectric interfaces. We use SPPs on metal-air interface to normalize the intensity of the slot mode. Numerical simulations (see Figure S2) confirm that the amplitude of the excited metal-air SPP does not significantly depend on the wavelength in the range of interest 1425-1525 nm and therefore the normalized slot mode intensity is proportional to the effective area.

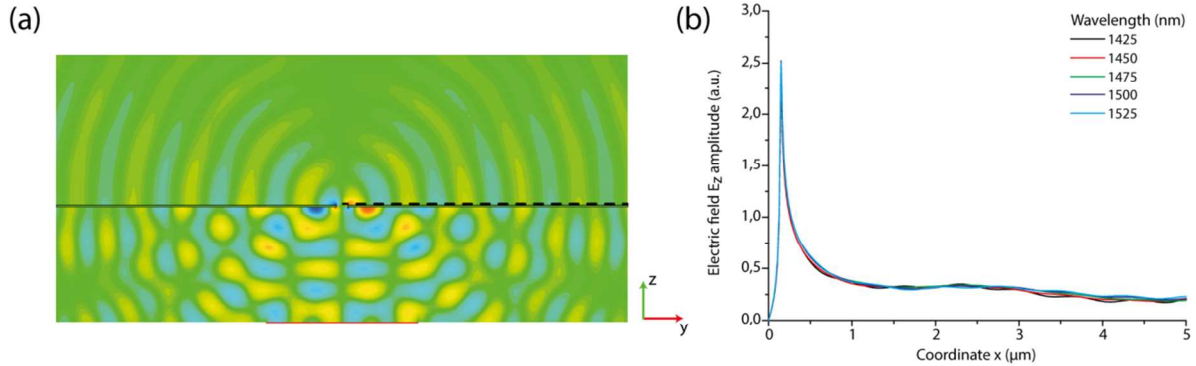


Figure S2. (a) Vertical electric field E_z (real part) distribution in the plane perpendicular to the slot. The y-polarized incident wave excites SPP on the air-metal interface upon diffraction through the slot. (b) Electric field E_z amplitude along the dashed line in the part (a) demonstrates that the intensity of the excited SPP does not significantly depend on the wavelength.

Fabrication. The waveguides and antennas were fabricated on a borofloat glass 500 μm thick substrate (Jinsol). ZEP 520 5.5% (in anisole) resist (thickness 150 nm) was used for electron beam lithography. To prevent charge accumulation a 20 nm thick Al layer was thermally deposited (Wordentec QCL 800). The resist was exposed with 100 kV JEOL JBX-9300FS electron beam lithography system at the charge dose 200 $\mu\text{C}/\text{cm}^2$. Then Al was removed with commercial MF-322 remover until no visible signs of metal were presented, and the resist was developed in ZED N50 developer for 120 s. Then 1 nm Cr and 49 nm Au were e-beam evaporated (Wordentec QCL 800). During the lift-off the sample was staying in hot acetone (50 C) upside down for 2 hours under constant stirring. Then slight ultrasound was applied for 2 minutes. Finally the sample was rinsed with acetone and isopropanol and carefully dried with nitrogen. After the fabrication we performed lateral size measurements with a scanning electron microscope (FEI Nova 600 NanoSEM and SEM Zeiss Supra 40 VP) and thickness measurements with an atomic force microscope (Dimension 3100 Bruker AXS). The values of the geometrical parameters of the fabricated structures and standard deviations are shown in Table S1. The SEM images of 0BA, 2BA and 2DA structures are shown in Figure S3.

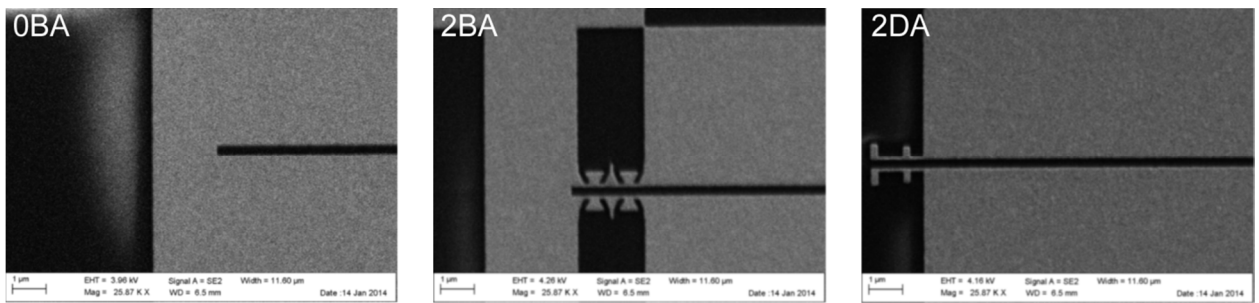


Figure S3. SEM microphotos of the fabricated 0BA, 2 BA and 2DA structures.

Field data processing. A main idea of filtering near-field data is that the recorded field resulted from the interference of two dominating modes: the slot mode propagating along the

waveguide, and SPP, excited on the edges of the waveguide and therefore travelling across it. However, there is a small difference in treating experimental and simulated near-fields, due to a slightly different excitation and measurement procedures. In our experiment the waveguides were illuminated with a defocused Gaussian beam, which can be described as following:

$$E(x, y) = E_0 \exp\left[-\frac{x^2 + y^2}{w^2(z)}\right] \exp\left[ik_0 \frac{x^2 + y^2}{2R(z)}\right] = E_0 \exp\left[ik_2 (x^2 + y^2)\right],$$

$$\left. \begin{aligned} w^2(z) &= w_0^2 \left[1 + \left(\frac{z}{z_R} \right)^2 \right] \\ R(z) &= z \left[1 + \left(\frac{z_R}{z} \right)^2 \right] \end{aligned} \right\} k_2 = \frac{k_0}{2R(z)} + \frac{i}{w^2(z)},$$

$$z_R = \frac{\pi w_0^2}{\lambda}, \quad k_0 = \frac{2\pi}{\lambda}$$

where E_0 is an electric field amplitude, λ is a free-space wavelength of illumination, $w_0 \approx 3 \mu\text{m}$ is a waist of the Gaussian beam, and $z \approx 65 \mu\text{m}$ is a vertical shift of the excitation parabolic mirror, used to increase the width of the illumination spot. Since only the sample is moving during the scan, the amplitude and phase of the Gaussian beam adjusted with the AFM tip will be changed at the position of the antenna during the scan change. Therefore, the measured amplitude of the slot mode will be in fact a convolution of the Gaussian beam profile and real propagation field. Then one can fit measured data with following:

$$E_{\text{measured}}(x, y) \rightarrow E_{\text{SPP}}(y) + E_{\text{slot}}(y) \exp[ik_{\text{slot}}x] \exp\left[ik_2 (x - x_0)^2\right]$$

where E_{measured} , E_{SPP} , E_{slot} , k_{slot} , k_2 are complex-valued functions and variables (taking into account amplitude and phase for E -field and propagation with decay for the k -vector), and x_0 is an effective coordinate of the antenna (in our fitting we assumed it to be $1 \mu\text{m}$ from the edge of continuous gold for 2BA and 2DA; for 0BA it was assumed to be at the beginning of the waveguide). In our fitting k_{slot} was a global fitting parameter (one for the whole image), while

E_{SPP} and E_{slot} were fitting parameters for each line along x-axis. The fitting was done in MATLAB by the least squares method with a use of the built-in MATLAB function *lsqcurvefit*. The results of the fitting for 2DA are shown in Figure S4, where the measured data, $E_{\text{measured}}(x, y)$ is denoted as RAW, the first term of fitting, $E_{\text{SPP}}(y)$, is denoted as SPP, the second term, $E_{\text{slot}}(y) \exp[ik_{\text{slot}}x] \exp[ik_2(x-x_0)^2]$, is denoted as Slot mode, and the difference, $E_{\text{measured}}(x, y) - E_{\text{SPP}}(y) - E_{\text{slot}}(y) \exp[ik_{\text{slot}}x] \exp[ik_2(x-x_0)^2]$, as Residual field.

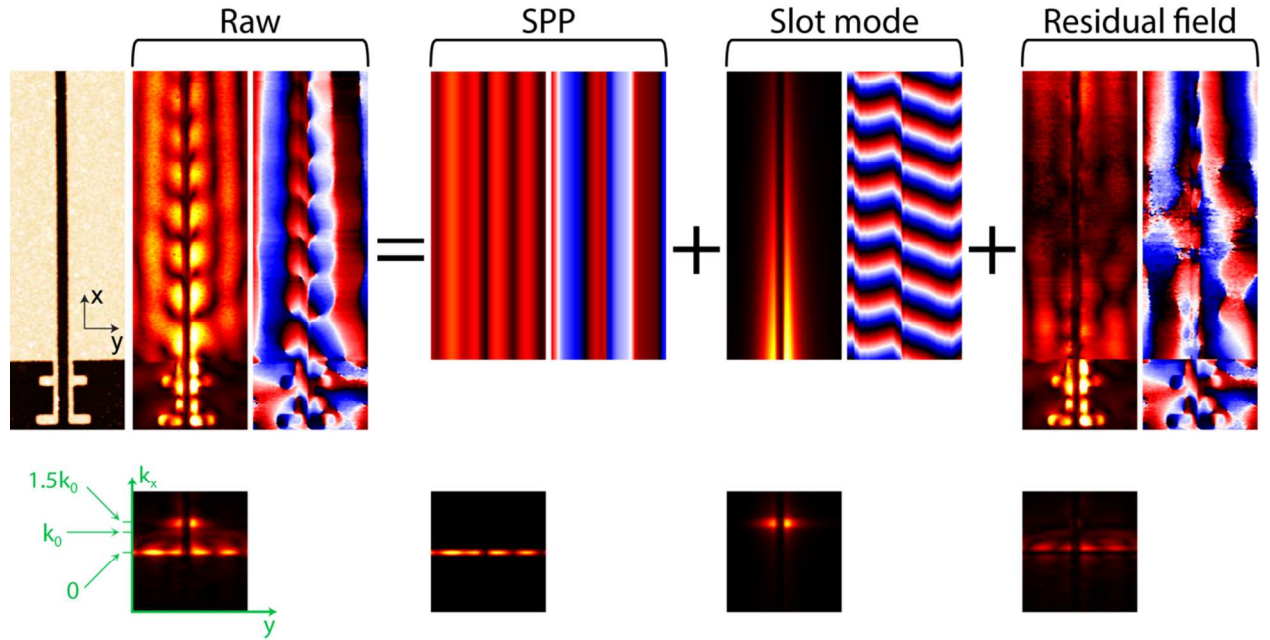


Figure S4. Fitting procedure shown on an example of 2DA. Top: Decomposition of the recorded Raw complex-valued data into fitted SPP, Slot mode, and Residual field. Bottom: the same procedure seen in k-space after applying 1D DFT along the waveguide (191×31 pixels, linearly interpolated to 191×200 pixels for clarity).

In order to present results concisely, we added the top part of Residual field (containing the waveguide) to SPP and showed it as the SPP background in our work [Figure 4 (e)-(g)], while the original near-field of the antenna (bottom part without waveguide), glued with fitted Slot

mode, is referred to as the slot mode field in our work [Figure 4 (h)-(j)]. The complete procedure of fitting is shown in Figure S4. One can note that there is still relatively large residual field near the beginning of the waveguide, which we ascribe to the excitation and propagation of the SPP, travelling partially along x -axis, due to the diffraction of the incident beam on the antenna and due to the edge effects for SPP, propagating across the waveguide. However, such distortion does not significantly influence the fitted slot mode and the filtering procedure, which is verified by a one-dimensional discrete Fourier transform (1D DFT) of the top part of complex-valued Raw, SPP, Slot mode, and Residual field along the waveguide (see bottom part of Figure S4). Note that due to a rather limited scanned area Fourier analysis does not allow to accurately determine waveguiding propagation constant k_{slot} .

Such fitting allowed determining propagation length and effective mode index of the slot mode for each wavelength [Figure 6(b)]. The normalized intensity of the slot mode was estimated as average value of squared E_{slot} , measured at the entrance of waveguide, x_1 , and normalized to the average value of squared E_{SPP} , i.e.,

$$I_{\text{slot}} = \frac{\int E_{\text{slot}}(y) \exp[ik_{\text{slot}}x_1] \exp\left[ik_2(x_1 - x_0)^2\right] dy}{\int E_{\text{SPP}}(y) dy}.$$

For 0BA, due to a weak slot mode, k_{slot} was fixed and determined by linear fitting of k_{slot} for 2DA and 2BA, so only the normalized intensity was determined during the fitting procedure.

As for the numerical simulations with plane wave excitation, the electrical field E_z , measured at 50 nm above the structure, appeared to contain substantial background of propagating light and SPP, excited on far edges of the sample due to diffraction. Such background negligibly influences the measurements of propagation constant and coupling efficiency, but creates a large obstacle for field filtering. Therefore, for near-field simulations, we used a cylindric Gaussian

beam (homogenous along x- and Gaussian along y-axis) to excite slot mode and cross-propagating SPP. The complete results of fitting the experimentally measured and numerically simulated near-field are presented in Figures S5 and S6, correspondingly.

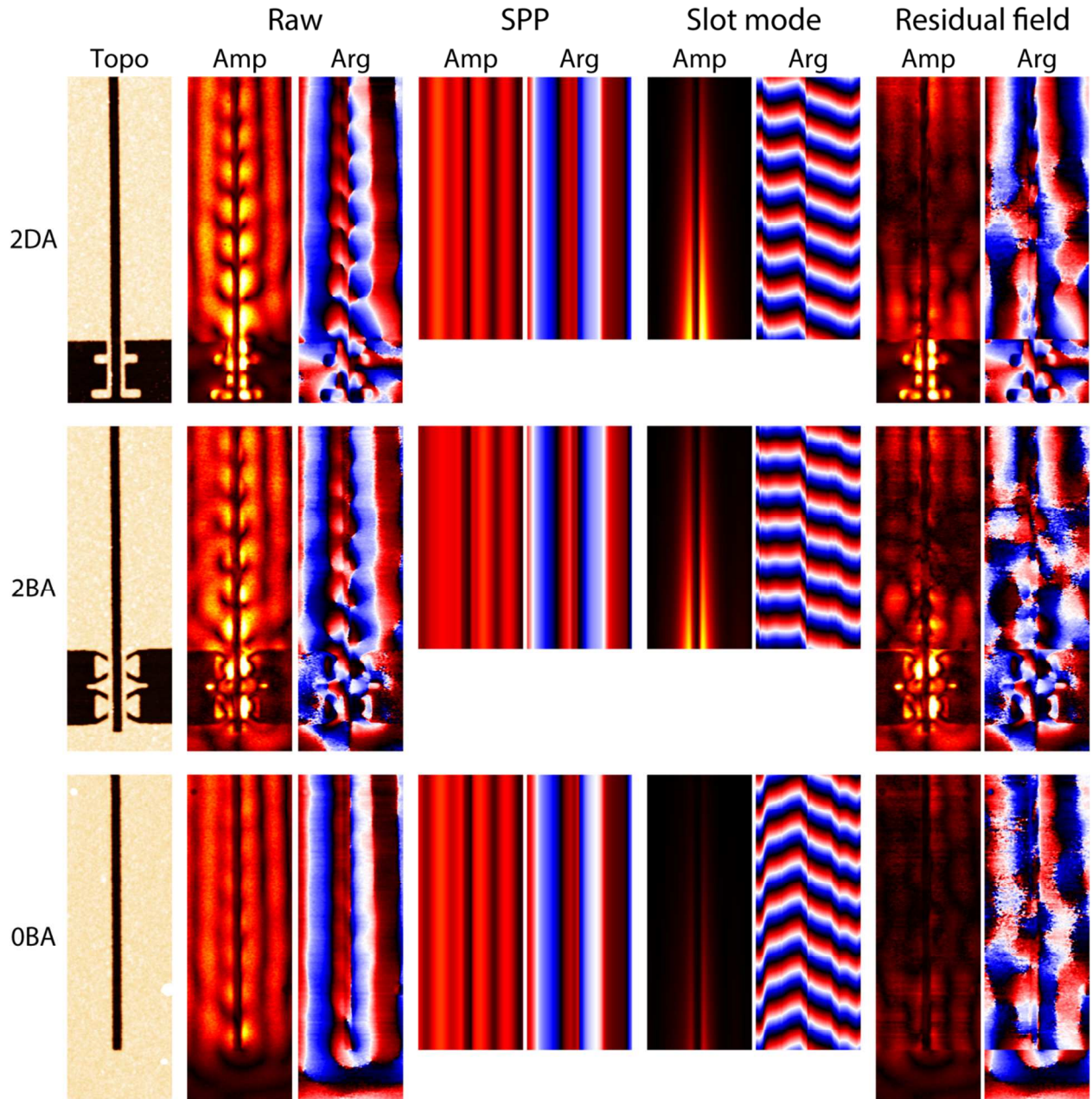


Figure S5. Results of fitting measured data for all measured antennas.

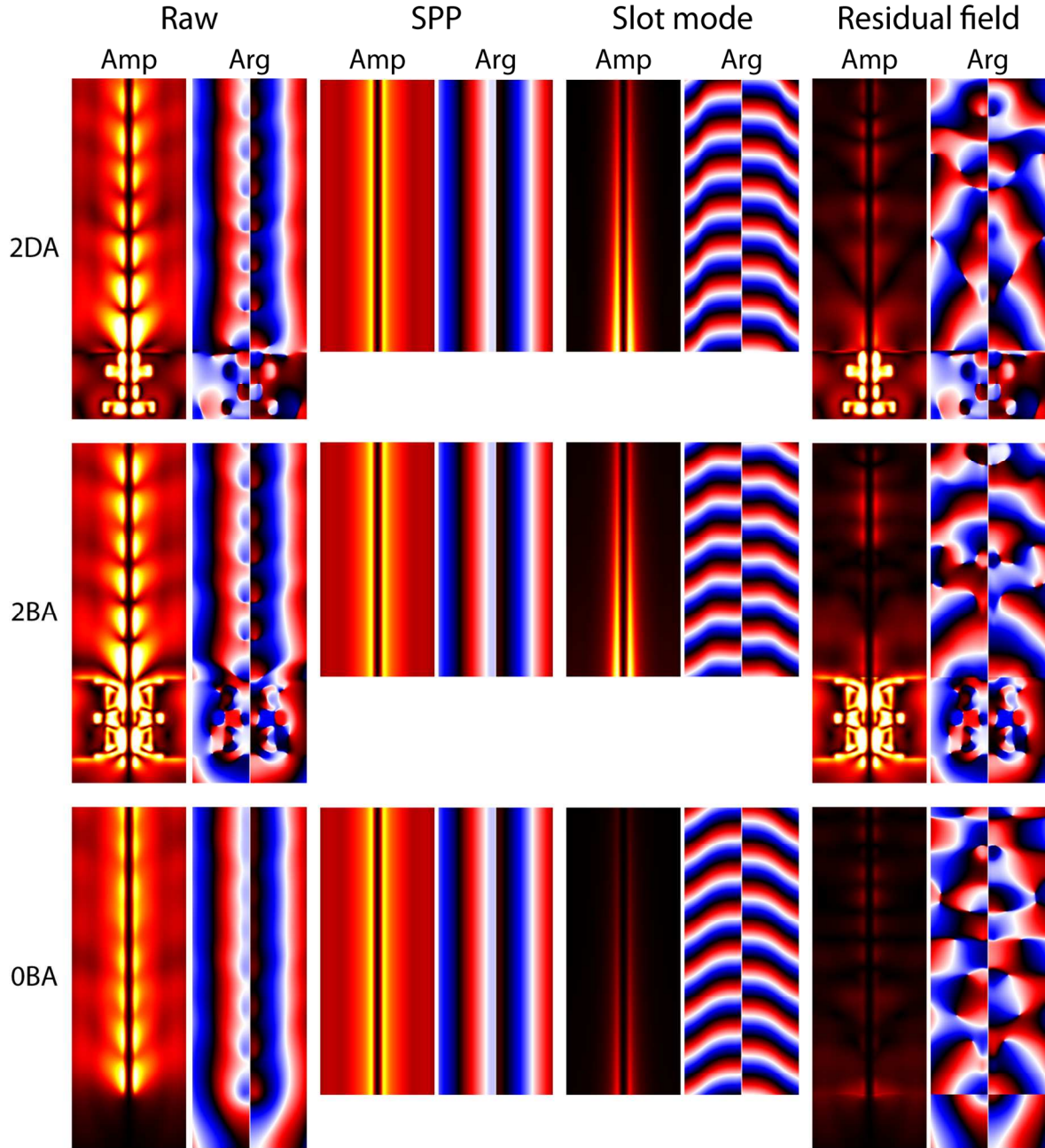


Figure S6. Results of fitting numerically simulated near-field.

References

- (1) CST. Computer Simulation Technology, AS <http://cst.com>.
- (2) Rakic, A D.; Djuricic, A. B.; Elazar, J. M.; Majewski, M. L.; Djuris, A. B. *Appl. Opt.* **1998**, *37*, 5271–5283.